# Predoped oxygenated defects activate nitrogen-doped graphene for the oxygen reduction reaction

Jiang, L.; Dijk, B. van; Wu, L.; Clément, M.; Hofmann, J.P.; Tudor, V.; ... ; Schneider, G.F.

**Note:** To cite this publication please use the final published version (if applicable).

# Predoped Oxygenated Defects Activate Nitrogen-Doped Graphene for the Oxygen Reduction Reaction

Lin Jiang, Bas van Dijk, Longfei Wu, Clément Maheu, Jan P. Hofmann, Viorica Tudor, Marc T. M. Koper, Dennis G. H. Hetterscheid,* and Grégory F. Schneider*

Cite This: *ACS Catal.* 2022, 12, 173−182

Read Online

ACCESS | Metrics & More | Article Recommendations | Supporting Information

**ABSTRACT:** The presence of defects and chemical dopants in metal-free carbon materials plays an important role in the electrocatalysis of the oxygen reduction reaction (ORR). The precise control and design of defects and dopants in carbon electrodes will allow the fundamental understanding of activity-structure correlations for tailoring catalytic performance of carbon-based, most particularly graphene-based, electrode materials. Herein, we adopted monolayer graphene — a model carbon-based electrode — for systematical introduction of nitrogen and oxygen dopants, together with vacancy defects, and studied their roles in catalyzing ORR. Compared to pristine graphene, nitrogen doping exhibited a limited effect on ORR activity. In contrast, nitrogen doping in graphene predoped with vacancy defects or oxygen enhanced the activities at 0.4 V vs the reversible hydrogen electrode (RHE) by 1.2 and 2.0 times, respectively. The optimal activity was achieved for nitrogen doping in graphene functionalized with oxygenated defects, 12.8 times more than nitrogen-doped and 7.7 times more than pristine graphene. More importantly, oxygenated defects are highly related to the 4e⁻ pathway instead of nitrogen dopants. This work indicates a non-negligible contribution of oxygen and especially oxygenated vacancy defects for the catalytic activity of nitrogen-doped graphene.

**KEYWORDS:** *monolayer graphene, nitrogen dopants, ORR activity, oxygenated vacancy defects, synergetic effect*
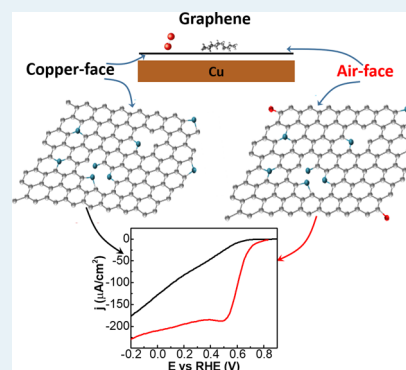
## INTRODUCTION

Nitrogen-doped (N-doped) carbon-based metal-free materials like graphene and carbon nanotubes are effective and promising alternatives to platinum catalysts for the oxygen reduction reaction (ORR), a critical reaction for renewable energy technologies in fuel cells.[1−4] A tremendous amount of experimental and theoretical effort has been devoted to determine the active sites of N-doped carbon materials for the ORR.[5−7] Nitrogen dopants in graphitic carbon materials, either pyridinic N[6,8] or graphitic N,[9] have been proposed to be potential active sites for ORR. Particularly, positively charged carbon atoms next to pyridinic nitrogen atoms in graphite have been suggested to preferentially adsorb $O_2$ molecules and thus favor fast ORR kinetics in acidic medium.[8,10] In contrast, pyridinic N-doped graphene is not ORR active.[6,11,12] On the other hand, a range of carbon defects and oxygen functional groups in carbon have exhibited an intriguing performance in catalyzing ORR.[13,14] For example, edged pentagon carbon defects are more active toward the ORR than N dopants in graphitic systems.[12,15] In part, the controversy of active sites for ORR in N-doped graphene can be ascribed to the significant variations in the structure and morphology of the studied materials, i.e., graphene nanoflake dispersions composed of multilayered nanosheets containing abundant oxygen groups, edges, and carbon defects.[16,17] Typically, the inhomogeneous active sites for ORR catalysis, caused by flake aggregation, irreversible pyrolysis, or vigorous chemical treatments, are less considered. Hence, it is of pivotal importance to systematically disentangle every element in the graphitic system that can contribute to the ORR activity.

In carbon materials, the origin of the catalytic activity resides in the electronic structure, which can be modulated by chemical doping and structure engineering.[18] Especially, when a carbon system is functionalized with multiple components — multilayered sheets in different sizes and crystallinities, heteroatom doping, and atomic defects — alternating the electronic structure, each can contribute individually and synergistically to the catalysis. For example, trace amounts of heteroatom doping like nitrogen have been reported to significantly boost the ORR activity of a defective graphene by tuning the electronic structure of the pentagon defects functioning as the active sites.[19] In addition, a theoretical study describing proton-coupled electron transfer on graphene

surfaces showed that carbene-type active sites are stabilized by a combination of pyridinic nitrogen and quinone-type oxygen functionalities.[20] Especially, oxygen groups are abundant in graphene nanoflakes and other carbon materials due to their high oxygen affinity. However, little experimental attention has been given to distinguish the individual roles of oxygen functionalities and carbon defects within N-doped carbon systems for ORR. The absence of a suitable model carbon catalyst with a well-controlled chemical composition and atomic structure has been the key limiting factor.

In this study, a graphene monolayer grown via the chemical vapor deposition (CVD) method was chosen as a model catalyst since it provides a reliable and well-defined $sp^2$ hybridized carbon surface.[21−23] Such a well-defined model catalyst is desired to disentangle the relationship between ORR activity and the atomic carbon structure upon heteroatom doping and carbon defects, all-in-all for the rational design of more efficient carbon catalysts. Here, the two sides of one graphene (G) surface, designated to be pristine G supported on a polymer and graphene on a glassy carbon electrode (G@ GC) in a disk-ring electrode system, demonstrate different ORR activity upon identical nitrogen doping treatments owing to the intrinsic difference in the surface oxygen-containing groups. Furthermore, nitrogen, oxygen, and vacancy defects were introduced into graphene in single-, dual-, and triple-doping modes, respectively. It is found that single-doped nitrogen in graphene has a limited effect on the ORR, while a synergetic effect of nitrogen with oxygen and/or defects remarkably enhances the activity. Especially, the highest activities achieved on the optimized triple-doped samples suggest a critical role of oxygenated defects in facilitating N-doped graphene for enhanced ORR. Moreover, the presence of nitrogen dopants in the functionalized carbon system is essential to boost the activity owing to their impact on the electronic structure.

## RESULTS AND DISCUSSION

**Structural Characterization of N-Doped Graphene.** Nitrogen dopants were systematically introduced into the basal plane of a monolayer graphene upon ammonia plasma treatments (details can be found in the Supporting Information). Raman spectroscopy, electron microscopy, and transport characterization were performed to reveal the impact of nitrogen dopants on the atomic and electronic structure of monolayer graphene. Raman spectroscopy (Figure 1a) was conducted to evaluate the N-doping process on chemical vapor deposition (CVD) graphene supported by a $SiO_2$/Si substrate. For pristine graphene, two main characteristic peaks for monolayer graphene can be found. The G peak ($\sim$1580 cm$^{-1}$) arises from the C−C stretching within all $sp^2$ carbon systems. As the overtone of the breathing modes of six-atom rings, the sharp 2D peak ($\sim$2670 cm$^{-1}$) is sensitive to the number of graphene layers and doping effects.[24] The monolayer crystallinity was also reflected in the high resolution transmission electron microscopy (HRTEM) images and the fast Fourier transform (FFT) pattern in Figure S1. After more than 2 s of nitrogenation, a D peak appears at $\sim$1340 cm$^{-1}$ (see Figure 1a) that corresponds to single phonon intervalley scattering events and is associated with the defects induced by the incorporation of nitrogen atoms into the lattice of graphene (i.e., nitrogen dopants and the edge defects).[25] Upon longer nitrogenation times ($t_N > 6$ s), a D′ peak at 1620 cm$^{-1}$ emerges as a shoulder of the G peak due to the

intervalley scattering induced by defects.[26] When $t_N$ increases from 0 to 60 s, the intensity ratio $I(2D)/I(G)$ decreases from 2.0 to 0.7 (Figure 1b) and the 2D peak shifts from 2674 to 2665 cm$^{-1}$ (Figure S2a); both are in line with an electron (n)-doping effect in nitrogenated graphene.[27−29] As a quantitative reflection of the defect density ($n_D$) and interdefect distance ($L_D$),[30] the ratio of $I(D)/I(G)$ in Figure 1c (black line) exhibits a similar growth trend with the peak widths (see $n_D$ and $L_D$ in Table S1). Such consistent saturation trends may correspond to the clustering of nitrogen dopants at a high doping level.[11,31] This is reflected by a domain-like defect distribution in graphene after 30 s of nitrogenation (Figure 1d). The full widths at half-maximum values (fwhm's) for the D, G, and 2D peaks (Figure S2b) slightly increase upon increasing $t_N$ from 0 to 30 s and are saturated at 60 s. The increase of the fwhm's indicates a growth of defect density. Specifically, the increasing trends for both the $I(D)/I(G)$ ratio and the fwhm of the G peak confirm the dominance of the $sp^2$-hybridized carbon network over the introduced defects; thus, we conclude that the N-doped graphene still has a high lattice integrity. It has been reported that a ratio of ca. 3 for $I(D)/I(D')$ represents boundary defects, while a ratio of ca. 7 indicates vacancy defects on the basis of a model of uniform defect distribution without clustering.[32] In our case, the $I(D)/I(D')$ ratios vary from 6.5 (10−20 s of nitrogenation) to 5 (more than 30 s of nitrogenation) (Figure 1c, blue dots), indicating that nitrogen dopants behave more like vacancy defects. To conclude, Raman spectroscopy shows that N-doped graphene has a high, uniform graphitization level and vacancy-like N dopants.

Next, we studied the electron transport characteristics of graphene in the configuration of an electrochemically gated graphene field effect transistor (GFET) that was fabricated following a previously reported strategy (see the Supporting Information).[33] We used an epoxy substrate to support a clean, pristine graphene surface that was protected by a clean and annealed copper substrate (Figure 1e). Moreover, this graphene surface was never in contact with (and thus not contaminated) any polymer that is generally used for graphene transfer[34] and was only exposed to ambient oxygen for a short period (within 24 to 48 h) before the measurements. Our previous work has confirmed that this graphene surface contains a lower density of charged impurities (i.e., originating from ambient oxidation or trapped impurities) than the polymer transferred one.[33] The conductance ($G$) of this clean graphene in Figure 1f (black line) demonstrates an ambipolar behavior with respect to the gate voltage ($V_g$). The $G$ ($V_g$) curves start to shift negatively after 10 s of nitrogenation, and the charge neutrality point (CNP) shifts by −30 to −60 mV between 20 and 60 s of nitrogenation. Such shifts suggest an n-doping effect in graphene (Figure 1g). Using the capacitor model in the electrochemical-gating configuration,[35] we extract the carrier mobility ($\mu$) of graphene, which decreases from $\sim$3800 to $\sim$550 cm$^2$ V$^{-1}$ s$^{-1}$ after 30 s of nitrogenation and subsequently levels off at 60 s of nitrogenation (Figure 1g, black). Notably, the high carrier mobility value for pristine graphene confirms its intrinsic high quality and low charge impurities. Consistent with the saturation trend of $I(D)/I(G)$ ratios in Figure 1c, the evolution of graphene carrier mobility is predicted to be closely related to the distribution of nitrogen dopants. At low doping levels ($t_N < 30$ s), nitrogen dopants independently implant into the carbon lattice, resulting in a rapid and dramatic conductivity degradation of graphene. At
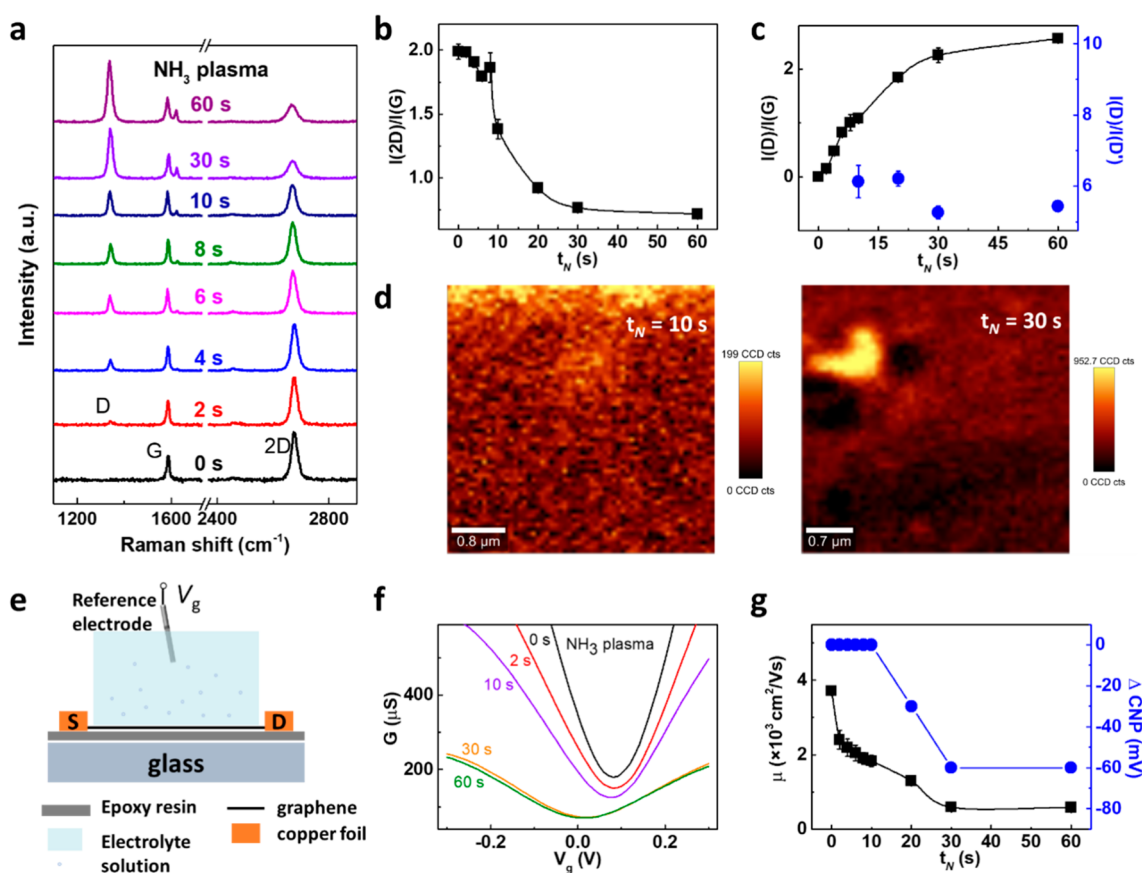
**Figure 1.** N-doping in monolayer graphene. (a) Raman spectra of graphene upon 0 to 60 s of nitrogenation using ammonia plasma. The spectra are recorded using 2.33 eV (532 nm) laser excitation. (b) Intensity ratio $I(2D)/I(G)$ as a function of nitrogenation times ($t_N$). (c) Evolution of intensity ratio $I(D)/I(G)$ (black) and $I(D)/I(D')$ (blue) with respect to $t_N$. (d) Raman mapping of the D band for graphene upon 10 and 30 s of nitrogenation. (e) Scheme of a liquid-gated graphene field effect transistor (GFET). S: source electrode; D: drain electrode. The electrolyte solution is 0.1 M KCl with 10 mM Tris (pH 8). (f) Conductance ($G$) vs the gate voltage ($V_g$) curves of graphene upon $t_N$ from 0 to 60 s. (g) The carrier mobility of graphene ($\mu$, black square) and charge neutrality point (CNP, blue dot) evolve with $t_N$. The error bars in panels b, c, and g are the standard deviations of the experimental values.

high doping levels (30 s < $t_N$ < 60 s), nitrogen dopants form clusters around the pre-existing nitrogen doping sites, resulting in a lower degree of conductivity degradation in graphene. These observations reveal that nitrogen dopants in the monolayer graphene lattice cause significant intervalley scattering, reduce the carrier mobility and conductivity, and induce an n-doping effect.

**Graphene Surface Preparation for ORR.** CVD graphene supported on the as-grown copper foil intuitively has two faces: one facing the copper foil (copper face) and the other facing the air (air face) (Figure 2a). As mentioned above, the copper face of graphene that has been previously confirmed to contain minimized impurities (i.e., oxidation, contaminations)[33] was adopted for the transport measurement (Figure 1e). To prepare monolayer graphene electrodes for ORR, both faces were employed according to the measurement configurations. In detail, the copper face was transferred onto the epoxy support (similar to the GFET device preparation), referred to as pristine G (Figure 2b), while the air face was transferred onto the glassy carbon (GC) electrode using a polymer,[34] referred to as G@GC (Figures 2c and S3). The slight differences in the original surface chemistry of the two graphene electrodes significantly determine their catalytic performance upon nitrogenation, which will be discussed further below.

X-ray photoelectron spectroscopy (XPS) was used to characterize the chemical structure of nitrogenated graphene. Figure 2d shows the XPS N 1s spectra for pristine and 30 and 60 s N-doped graphene. The N 1s spectra for 30 s N-doped samples consist of two main peaks centered at 398.9 and 399.9 eV, corresponding to pyridinic (pyrid-) and pyrrolic (pyrro-) N.[12,36] For 60 s N-doped graphene, in addition to the pyrid- and pyrro-N peaks, another peak at 401.1 eV is observed and assigned to graphitic (graph-) N. Correspondingly, the XPS C1s spectra for pristine and 30 and 60 s N-doped graphene are shown in Figure S4. The N/C and O/C ratio increases respectively from 2.0% and 9.0% for 30 s to 3.1% and 21% for 60 s of nitrogenation. Moreover, the dominant forms of pyrid- and pyrro-N agree well with the observed n-type doping effect in Figure 1.[37,38]

The ORR activity was first studied with pristine G supported on the epoxy substrate for both acid and alkaline media. Figure S5a–d shows the cyclic voltammograms (CVs) of pristine G in 0.1 M $H_2SO_4$ and 0.1 M NaOH solution saturated with Ar and $O_2$, respectively, in a stationary configuration. A more positive onset potential in alkaline medium (~0.68 V) than in acidic medium (~0 V) and a higher current density (~4-fold at −0.2 V vs reversible hydrogen electrode (RHE)) in 0.1 M NaOH shows a higher ORR activity in alkaline medium. It is well-known that carbon-based catalysts are more active for the ORR
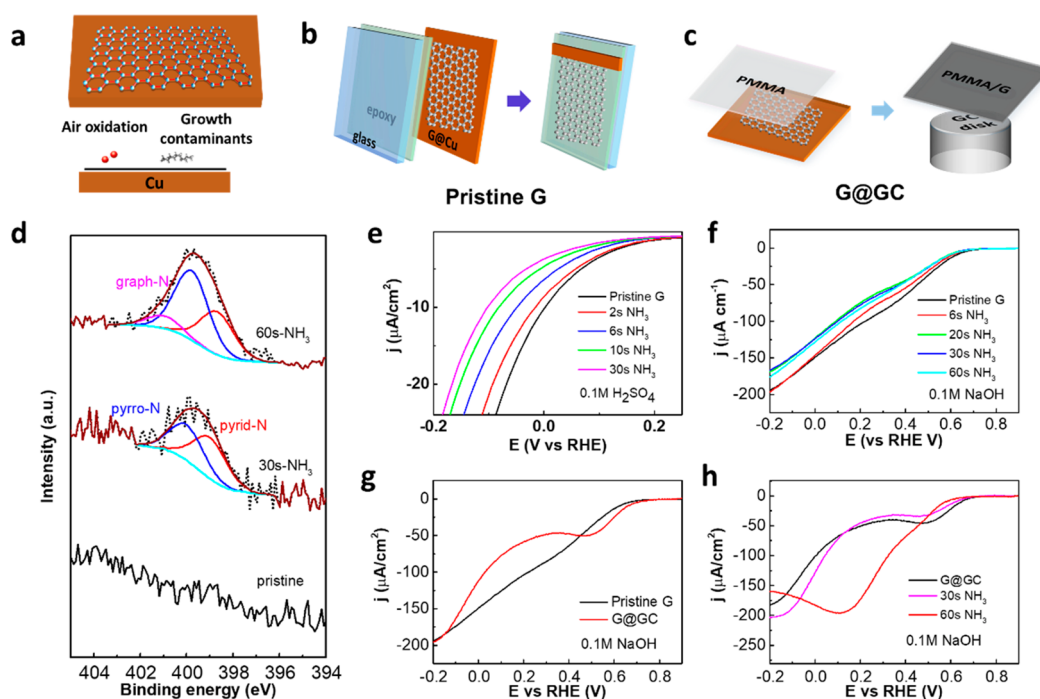
**Figure 2.** Graphene electrode preparation for ORR. (a) Illustration of the asymmetrical surface of CVD graphene film: air face and copper face. (b) Preparation of pristine G supported by an epoxy substrate using the copper face of graphene. (c) Preparation of G@GC using the air face of graphene. (d) N1s core level spectra of pristine G and 30 and 60 s N-doped graphene. (e) Linear sweep voltammetry (LSV) polarization curves of graphene upon 0 to 30 s of nitrogenation in $O_2$-saturated 0.1 M $H_2SO_4$. (f) LSV curves of graphene upon 0 to 60 s of nitrogenation in $O_2$-saturated 0.1 M NaOH. (g) LSV curves of a pristine G and G@GC. (h) LSV curves of G@GC before and after 30 and 60 s of nitrogenation. All nitrogenation treatments were performed using ammonia plasma.

in alkaline media. This is most likely due to $O_2^{-\bullet}$ being the first intermediate in the mechanism of ORR, which is formed by an electron transfer reaction that is not coupled to proton transfer and therefore does not scale linearly with the RHE reference scale.[39]

The LSV curves in alkaline medium have an extra reduction peak at ca. 0.45 V. This peak is ascribed to oxygen reduction catalyzed by the oxygen-containing groups present on the surface of graphene and other carbon electrodes including glassy carbon.[40] In addition, more aged pristine G showed increased current in this region (Figure S5c). Therefore, only graphene samples producing similar low peak currents at 0.45 V with the LSV in Figure 3a were used for doping treatment studies. Upon nitrogen doping from 0 to 60 s, the catalytic current densities are observed to decrease monotonically both in acidic (Figure 2e) and in alkaline medium (Figure 2f). It differs from earlier reports claiming that n-doping of nitrogenated graphene improves ORR activity by creating Lewis basic sites, which enhance initial $O_2$ adsorption.[5,8] In our case, the observed decrease in ORR activity of graphene after nitrogenation suggests that the N-doping sites within the graphene surface do not contribute to the generation of active catalytic sites. Such an observation is supported by recent reports that the catalytic activity of graphene decreases upon nitrogenation.[11,12] For example, N-doped graphene was reported to show similar ORR activity with pristine graphene.[12] A theoretical study proposes that the nitrogen atoms in N-doped graphene could actually hinder the adsorption of oxygen molecules onto the graphene surface due to their higher electron density.[41]

Furthermore, the air face of CVD graphene as the opposite face of pristine G was transferred onto the GC disk electrode,

which is part of the rotating ring-disk electrode (RRDE). Two types of graphene samples on GC support were prepared (Figure S3) and compared for their ORR performance (Figure S6a). A monolayer graphene on the GC disk (denoted as G′@GC) decreases the ORR current compared to that of bare GC, indicating that fewer active sites are available on the graphene surface (Figure S6a). Furthermore, bilayer graphene on GC (namely, G@GC) has an even more reduced ORR current compared to G′@GC. This implies that GC as the underlying substrate has a certain influence on the catalysis of the graphene overlayer, for instance, through cracks in this monolayer graphene film. In contrast, G@GC displays reliable reproducibility and is reliability reflected by LSV curves and Raman spectra (see Figure S6b−d and Section S2.3) before and after rotation tests. Therefore, G@GC was used for the RRDE measurements (vide infra). Compared to the LSV of pristine G, G@GC (at 0 rpm) has a more pronounced peak at 0.45 V (Figure 2g). As previously described, this feature is probably related to a higher surface oxidation of G@GC as compared to pristine G. Of note, G@GC exhibits a slightly increased current after 30 s of nitrogenation and significantly boosted activity after 60 s of nitrogenation, which is in high contrast to that on pristine G (Figure 2h). Given the decrease of conductivity versus the increase of ORR activity in N-doped graphene, it is concluded that the degraded conductivity of the graphene upon the employed doping conditions (~600 $cm^2$ $V^{-1}$ $s^{-1}$ for 30 to 60 s of nitrogen doping) is not necessarily the limiting factor for ORR catalysis.

Such differences in ORR activity between the two faces of the same monolayer graphene can be attributed to the different surface chemistry and underlying substrates between pristine G and G@GC. For the substrates, the GC electrode can only
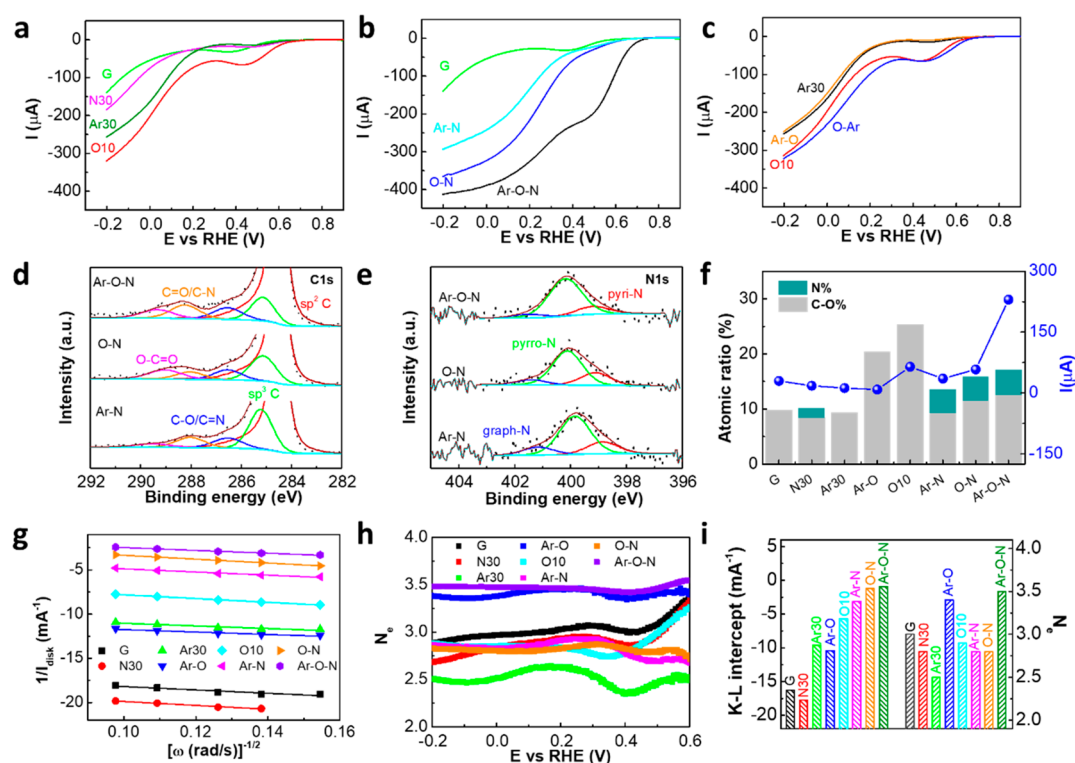
**Figure 3.** ORR activity correlates with chemical compositions on G@GC. (a) LSV curves of G, N30, Ar30, and O10 samples at a rotation speed of 800 rpm. N30 represents 30 s of nitrogenation using ammonia plasma, Ar30, for 30 s of argon plasma treatment, and O10, 10 s of oxygen plasma treatment. (b) LSV curves of G, Ar−N, O−N, and Ar−O−N samples. Ar−N represents graphene codoped with Ar30 and N30; O−N is for O10−N30 and Ar−O−N, for Ar30, O10, and N30 treated graphene. (c) LSV curves of O−Ar and Ar−O in comparison to their monodoping counterparts. (d) C1s core level XPS spectra of Ar−N, O−N, and Ar−O−N. (e) N1s core level spectra of Ar−N, O−N, and Ar−O−N. (f) ORR activity at 0.4 V correlates with atom% of carbon−oxygen and carbon−nitrogen (C−O% + N%) for non-, single-, and dual-doped graphene samples. (g) Koutecky−Levich (K-L) plots and linear fits of the inverse of the limiting currents at 0.1 V vs RHE for different doped graphene samples versus the inverse square root of the rotation rates. (h) Electron transfer number, $N_e$, of differently doped graphene samples at various potentials. (i) K-L intercept extracted from panel g and $N_e$ comparisons for differently doped graphene. All the ORR experiments were performed in 0.1 M NaOH solutions saturated with $O_2$ at a rotation speed of 800 rpm (scan rate of 100 mV/s).

contribute to the ORR of G@GC if cracks or holes were introduced during the transfer process. To test this possibility, the ORR currents of G@GC after 60 s of nitrogenation (N60), partially exposed GC electrodes (from 10% to 50% in terms of area), and a fully exposed bare GC were compared (Figure S7). Due to the large amounts of carbon defects and oxygen functionalities, bare GC exhibits a distinct polarization curve with a prominent extra peak at ca. 0.45 V. In comparison, N60 exhibits a much larger ORR current at a higher overpotential (∼0−0.2 V vs RHE) and a relatively lower current at 0.45 V compared to all partially exposed GC electrodes. Such a difference indicates that the underlying GC substrate plays a negligible role in the ORR activity of N60. Therefore, the surface chemistry of graphene upon nitrogenation should be mainly responsible for the observed difference in ORR activity. As confirmed by XPS (Figures 2d and S4) and the ORR performance (Figure 2h), surface-containing oxygen groups are expected to play a critical role in boosting the catalytic properties of graphene upon N-doping. Inspired by recent works in which oxygen-containing groups[5,8] and carbon defects[15,19,42] in carbon-based materials were found to be closely related to the active ORR performance, we further investigated the activities of graphene doped or codoped with nitrogen and oxygen as well as vacancy defects, which can intrinsically or unintentionally be present in carbon materials.

**Activity Correlations in Activated N-Doped Graphene.** We used a rotating ring-disk electrode (RRDE) method to gain insights into the ORR kinetics and activity of nitrogenated graphene. The current was measured at both the glassy carbon (GC) disk and the platinum ring. The Pt ring was held at a potential of 1.2 V to oxidize ORR products such as hydrogen peroxide $HO_2^-$ (the form of $H_2O_2$ in alkaline medium) and/or superoxide $O_2^{-\bullet}$ with a collection efficiency of 22.5% (Figure S8 and Section S2.4). G@GC was continued for individual and cooperative doping of nitrogen (30 s nitrogenation, N30), vacancy defects (30 s argon plasma, Ar30), and oxygen (10 s oxygenation, O10) to compare their synergy effects on the ORR. The doping levels for N30, Ar30, and O10 were controlled using comparable defect densities reflected by Raman spectra (Figure S9). The dual-doping and triple-doping graphene samples were simply denoted as O−N (O10 followed by N30) and Ar−O−N (Ar30 followed by O10 and last N30), respectively. In particular, the original G@GC without any doping treatment was simplified as G.

Furthermore, ORR activities are evaluated on the basis of the kinetic catalytic currents obtained at potentials where the diffusion limited condition is not yet achieved. Before that, the CV curves for G@GC samples in a 0.1 M NaOH solution purged with argon and oxygen shown in Figure S10 confirmed the ORR current. The stable ORR current was obtained after ten CV scans in an oxygen saturated solution (Figure S11). As

shown in the LSV curves at a rotation speed ranging from 400 to 1000 rpm in Figure S12, nondoped, single-doped, and dual-doped graphene samples are less active at potentials between 0.1 and 0.4 V vs RHE, while the triple-doped sample (Ar−O−N) is more active with more positive potentials between 0.4 and 0.6 V vs RHE. Therefore, the currents at 0.4 V vs RHE were selected for the activity comparison between different samples. However, the ORR currents at 0.4 V vs RHE for the less active graphene samples can be influenced by the oxygen-containing groups (the extra reduction peak at 0.45 V vs RHE). Correspondingly, the currents at 0.2 V vs RHE were also compared to gain more reliable insights into the activity trends for less active samples (see Figure S13). Compared with G in Figure 3a, N30 exhibits a similar or even lower current (~0.6-fold@0.4 V, ~1.2-fold@0.2 V), indicating a limited effect of N-doping alone in the graphitic surface on ORR. Ar30 samples show similar levels of activity (~0.1-fold) at 0.4 V vs RHE and slightly higher activity (~1.4-fold) at 0.2 V vs RHE. Meanwhile, O10 has a much higher activity (2.2-fold@0.4 V, 2.9-fold@0.2 V) with a higher onset potential of 0.63 V compared with that of G at ~0.5 V. Such differences suggest that vacancy defects and oxygen dopants are more ORR active than nitrogen dopants in graphene. In Figure 3b, Ar−N and O−N show more enhanced activities (~1.2- and ~2.0-fold@0.4 V, respectively) than N30 alone, while Ar−O−N plateaus the activity up to ~7.7-fold of G with the largest onset potential of 0.7 V. Of note, O10 has even higher improvement than Ar−O and Ar−N, which can be associated with the contribution of oxygen-containing groups featured at 0.45 V. Importantly, the significant activity enhancement in Ar−O−N compared to other single- or dual-doping samples (N30, Ar−N, O−N) indicates the activation roles of oxygenation and vacancy defects for N-doped graphene with enhanced ORR activity. Notably, the active carbon atoms (i.e., carbene-type) adjacent to N and O heteroatoms are regarded as the active sites for ORR catalysis.[8,43] Specifically, these contiguous heteroatoms or defects contribute to lowering the thermodynamic and kinetic barriers of the active carbon atoms for ORR. Therefore, the activation role herein refers to a process where the presence of oxygen dopants and/or defects lowers the energy barriers for ORR in N-doped graphene. With the absence of oxygen dopants or defects, nitrogen dopants alone do not lower the barriers sufficiently for ORR. Further control tests in Figure 3c compare Ar−O and O−Ar with their single-doped counterparts, namely, Ar30 and O10. The similar polarization behaviors of Ar−O vs Ar30 and O−Ar vs O10 suggest that the combination of vacancy defects and oxygen dopants shows little cooperative effect for enhanced ORR. Meanwhile, it also suggests the essential contribution of N-dopants in promoting ORR activity of graphene samples doped with oxygen dopants or defects.

Given the evident synergistic effect from N and O dopants and vacancy defects in dual- and triple-doped graphene, we particularly focused on the comparison of chemical compositions for Ar−N, O−N, and Ar−O−N and the correlation with their ORR activities. XPS C1s and N1s spectra for Ar−N, O−N, and Ar−O−N are displayed in Figure 3d,e. In particular, the C1s peak is adopted rather than the O1s peak for the analysis of O content due to the following reasons: (i) the O1s signals may include complicated contributions from copper oxide (growth substrate), surface adsorbents, or contamination (surface/interface); (ii) the C1s peak contains all the chemical bonding information on carbon mainly originating from

graphene, which can be confirmed by the dominant sp² C ratio in each graphene sample. The C1s spectra can be deconvoluted into five peaks: sp² C−C (284.4 eV), sp³ C−C (285.0 eV), C—O/C═N (286.4 eV), C═O/C—N (288.0 eV), and O—C═O (289.0 eV), respectively.[36,44] In addition to the dominant sp² C, Ar−O−N contains the highest C═O/C—N content (6.7%) while Ar−N has the most sp³ C content (17.8%). As shown in N1s spectra, the three typical N dopants, namely, pyrid-N (398.9 eV), pyrro-N (399.9 eV), and graph-N (401.1 eV), exist in all three samples. The highest atom% for pyridinic N, pyrrolic N, and graphitic N is found, respectively, in O−N (1.1%), Ar−O−N (3.5%), and Ar−N (0.6%). In addition, XPS characterizations were also conducted for other single-doped (Ar30, O10) and dual-doped (Ar−O) samples (Figure S14) for comparison.

To gain a deeper understanding of the origin of the enhanced activity, we further investigated the relations between chemical composition and catalytic performance. Derived from the LSV data in Figure 3a−c, ORR activities (at 0.4 V vs RHE) rank from low to high in the order of nondoped G, single-doped N30 and Ar30, dual-doped Ar−O, single-doped O10, and dual- and triple-doped Ar−N, O−N, and Ar−O−N in Figure 3f. After the atom% of different functionalities in graphene samples are analyzed (see Table S2), the sum contents of carbon−oxygen (C−O%, gray column) and nitrogen (N%, green column) are found to be positively correlated to ORR activities of graphene after excluding the extra contribution of oxygen-containing groups in oxygen plasma treated samples. The highest current at ~0.45 V of O10 compared to other samples, illustrated in Figure 3a, is further confirmed by the highest oxygen content and superior ORR activity for O10 shown in Figure 3c. It is of note that the Ar−O sample has a much higher C−O% than Ar30 but a similar (@ 0.2 V in Figure S13) or even lower activity (@0.4 V in Figure 3f). Therefore, it is hypothesized that the contributions of oxygen dopants and vacancy defects to ORR do not have a synergetic effect. Oxygenation as the final doping treatment (i.e., Ar−O and O10) results in relatively higher carbon−oxygen atom% (~20%) in graphene, which is in high contrast to nonoxygenated samples (~8.6−9.9% for G, N30, and Ar30) and oxygenated samples followed by nitrogenation (~12.6−13.3% for O−N and Ar−O−N). In addition, the higher N atom% in dual-doped samples (O−N, Ar−N) compared with N30 suggests that oxygenated groups in graphene can enhance the doping levels of the following nitrogenation. Meanwhile, the N-doped graphene samples (Ar−O−N, O−N, and Ar−N) generally contain lower oxygen contents but much higher ORR activity than the non-nitrogenated graphene (Ar−O and O10), suggesting that relatively low atomic ratios of oxygen groups in graphene are sufficient to activate the ORR activity of N-doped graphene. Also, the presence of N dopants in N-doped samples versus the non-N-doped counterparts (i.e., N30 vs G, Ar−N vs Ar−O, O−N vs O, Ar−O−N vs O−N) further confirm the critical contribution of N-dopants for ORR (Table S2), but the similar N atom% for Ar−N (~4.4%), O−N (~4.4%), and Ar−O−N (~4.5%) samples also suggests that ORR activity is not purely dependent on the content of N-dopants in graphene. Therefore, we assumed that N-doping in graphene is not sufficient to catalyze ORR. In other words, oxygen codoping is essential to activate N-doped graphene for ORR activity. Meanwhile, the ratios between N% and C−O% ranging from 0.2 for N30 to 0.44 for Ar−N, 0.35 for O−N, and 0.34 for Ar−O−N indicate that a balanced doping proportion between N
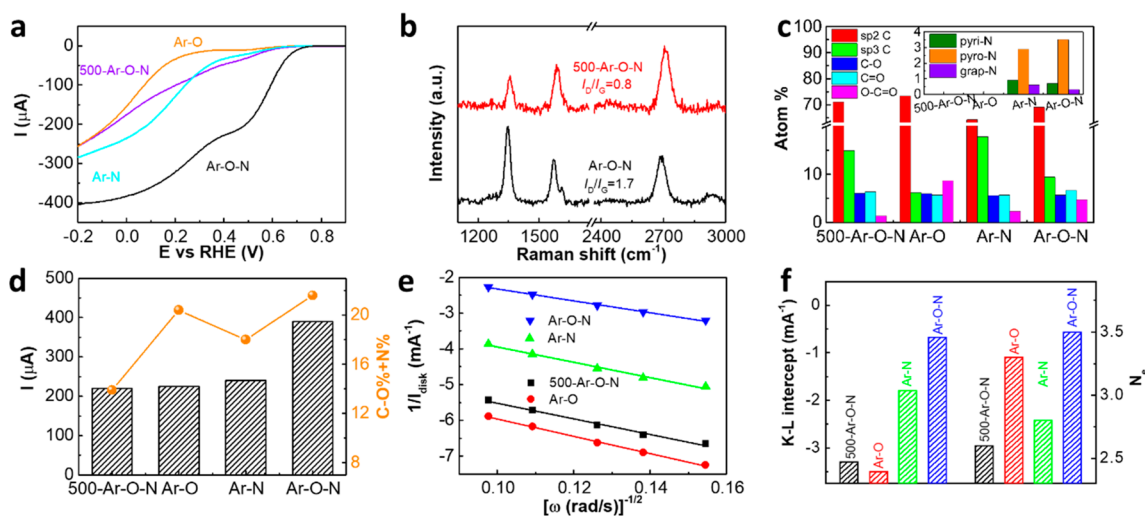
**Figure 4.** Specific roles of vacancy defects and oxygen and nitrogen dopants in ORR. (a) LSV curves of Ar−O−N before and after annealing (500−Ar−O−N), Ar−O, and Ar−N. (b) Raman spectra of Ar−O−N and 500−Ar−O−N. (c) Atom% comparisons of 500−Ar−O−N, Ar−O, Ar−N, and Ar−O−N. (d) Correlations of ORR activities with atomic% of carbon−oxygen and carbon−nitrogen (C−O% + N%) for 500−Ar−O−N, Ar−O, Ar−N, and Ar−O−N. (e) K-L plots of 500−Ar−O−N, Ar−O−N, Ar−O, and Ar−N at 0 V. (f) K-L intercept extracted from panel d and $N_e$ comparison for 500−Ar−O−N, Ar−O, and Ar−N, and Ar−O−N. All the ORR experiments were performed in 0.1 M NaOH solutions saturated with $O_2$ at a rotation speed of 800 rpm (scan rate of 100 mV/s).

and O dopants should lead to higher ORR activities in graphene. Compared with N30, Ar−N exhibits a 2-fold activity with the same O% and 2.5-fold N%; O−N has 3.2-fold activity with 3% higher O% and 2.5-fold N%; Ar−O−N has 12.8-fold activity with 4.2% higher O% and 2.5-fold N%. The comparisons also support that (1) predoped vacancy defects or oxygen dopants can cause a higher N% in graphene and higher ORR activity; (2) at the same levels of defects and N%, more O% contributes to higher activity.

A Koutecky−Levich (K-L) analysis of the RRDE data was performed to further compare the activity and the electron transfer number, $N_e$, respectively (Figure 3g−i). The currents at 0.1 V vs RHE for different graphene samples were collected for the K-L analysis. The linear fits for the inverse of the currents at 0.1 V vs RHE versus the inverse square root of the rotation rates in Figure 3g confirm the K-L behavior. The K-L intercepts can be used to compare the activities for different graphene samples using the intersection at the axis of $1/I_{disk}$, which corresponds to the kinetics current ($I_K$). A higher $I_K$, a direct indicator of a higher catalytic activity, will be reflected by a value of the $1/I_{disk}$ intersection closer to zero. The intercepts of the K-L plots summarized in Figure 3i are consistent with the summary of the activities in Figure 3f, which further supports the correlation between ORR activity and atomic ratios. Using the ring current $I_r$ and disk current $I_d$ collected from the RRDE data (see Figure S10), the electron transfer number $N_e$ can be derived using eq 1

$$N_e = 4I_d/(I_d + I_r/N) \tag{1}$$

where $N$ is the current collection efficiency of the ring electrode (see Figure S8). As shown in Figure 3h, $N_e$ at various potentials for different graphene samples ranges from 2.5 to 3.5. Figure 3i further summarizes the averaged $N_e$ in the potential range of −0.2 to 0 V where the diffusion-limited current is basically achieved. Ar30 exhibits the lowest $N_e$ number of 2.5, while Ar−O and Ar−O−N shows the highest number of 3.4 to 3.5. Other samples display similar $N_e$ numbers at the range of 2.8 to 2.9. Such contrasts in Ar30

versus Ar−O and Ar−O−N suggest that oxygenated defects can be the active sites responsible for water production, while vacancy defects alone favor more hydrogen peroxide production. Given the similar N doping levels in Ar−N, O−N, and Ar−O−N, as well as the similar $N_e$ for Ar−O and Ar−O−N, it is concluded that nitrogen dopants should have little contribution to the 4e⁻ ORR pathway.

When one takes both the effects of dopants and vacancy defects into consideration, it is hypothesized that oxygen dopants in the vicinity of vacancy defects in graphene create the active sites for the 4e⁻ pathway, while oxygen dopants are essential to activate N-doped graphene for ORR activity. The novel finding in this work is that the intentional or unintentional doped oxygen groups in the lattice of monolayer graphene are the prerequisite for the N-doped carbon system to show enhanced ORR activity. In brief, the predoped oxygenated defects create the activation center integrating nitrogen heteroatoms (illustrated in the scheme in Figure S14a) to lower the kinetic barrier of the active sites in graphene, thus enhancing the ORR activity and selectivity toward water production. Further incorporation of nitrogen dopants contributes to optimize the electronic structure of the predoped graphene system. Moreover, the atom ratios of nitrogen versus oxygen dopants (0.2 < N/O < 0.35) are critical for achieving the optimized ORR performance of doped graphene. On the one hand, our highlight for oxygen groups in N-doped graphene for ORR catalysis is also supported by a recent work identifying the 4e⁻ ORR active sites as $sp^2$ carbons that are located next to oxide regions in nitrogen-doped reduced graphene oxide.[45] In contrast, our work focuses on systematically disentangling the roles of potential elements involving carbon defects and oxygen and nitrogen dopants in contributing to the ORR reaction using a well-defined graphitic surface of graphene. On the other hand, the contribution of nitrogen heteroatoms in predoped graphene for improved ORR activity in our work is partially in line with recent reports on defective carbon materials.[19,42] However, the oxygen contents that may intrinsically exist in the materials or are

unintentionally introduced during chemical processing are not taken into account in these previous reports. In contrary, our work constructively fills in the gap in understanding the critical roles of oxygen dopants for ORR in N-doped carbon systems with or without defects.

**Specific Roles of Dopants and Defects for ORR.** An annealing treatment for Ar−O−N samples was performed to further confirm the critical contributions of oxygenation and vacancy defects to activating N-doped graphene for ORR. Figure 4a displays the LSV curves of Ar−O−N before and after 500 °C annealing (denoted as 500−Ar−O−N; see the Supporting Information for details) in comparison with Ar−O and Ar−N. It is evident that the annealing treatment significantly reduces the current of Ar−O−N to the levels between Ar−O and Ar−N and decreases the onset potential to be similar to that of Ar−N (∼0.57 to 0.59 V). The annealing treatment was expected to remove some functional groups in Ar−O−N samples and result in low defect density. Correspondingly, Raman spectra show that the defect density reflected by the $I(D)/I(G)$ ratio drops from 1.7 for Ar−O−N to 0.8 for 500−Ar−O−N (Figure 4b). Moreover, N1s spectra of 500−Ar−O−N (Figure S14) shows the absence of N-dopants and an obvious rise in the atom% of sp$^3$ C compared to Ar−O−N (from 9.4 to 14.9, Figure 4c and Table S2). Therefore, it is assumed that the decrease of defect density should be related to the removal of N-dopants. Moreover, the absence of nitrogen and the decreased activity in annealed samples support the essential role of nitrogen dopants in graphene predoped with oxygenated defects for ORR. In addition, the increase of sp$^3$ C species could originate from the hydrocarbon contaminations during the annealing process rather than chemical functionalities in the graphene surface considering the evident decrease in defect density. Importantly, the activity of 500−Ar−O−N correlates well with the sum contents of carbon−oxygen (C−O%) and nitrogen (N%) in comparison with other nonannealed samples (Figure 4d). Further Koutechy-Levich analysis in Figure 4e,f reveals that activities reflected by the K-L intercepts agree well with the current values in Figure 4d. For the electron transfer number, $N_e$, 500−Ar−O−N exhibits the lowest number of 2.6, lower than 2.8 for Ar−N and 3.3 for Ar−O (Figure 4f). As discussed above that oxygenated defects are most likely related to the 4e$^-$ pathway, 500−Ar−O−N is expected to contain less active oxygenated defects due to atomic reconfiguration or contamination coverage induced by the annealing treatment.

Vacancy defects and oxygen and nitrogen dopants were doped in different orders into graphene to further evaluate their specific roles in improving ORR (Figure S15). The comparison in Figure S15a shows that O−N exhibited a higher activity than N−O over a wide range of overpotentials (0.4 to −0.2 V). Such a contrast is closely related to the different compositions. The much lower oxygen content in O−N (11.5%) than that in N−O (18.7%) supports that a higher ORR activity in graphene should benefit from an optimal proportion between N and O dopants. Meanwhile, the 2-fold nitrogen content in O−N (4.4%) compared to that in N−O (2.2%) indicates that predoped oxygen dopants favor the incorporation of the nitrogen dopant in the graphene lattice. Therefore, the comparison further confirms that predoped oxygen dopants in graphene are beneficial for a higher nitrogen doping level and a higher ORR activity. Nitrogenation in graphene samples predoped with oxygenation and vacancy defects (Ar−O−N and O−Ar−N) still contribute to higher

activities (Figure S15b). In comparison, nitrogenation followed by oxygenation and vacancy introduction, namely, N−Ar−O and N−O−Ar, contribute to relatively lower activities. Such contrasts confirm that oxygen and vacancy predoped graphenes are more beneficial to improve ORR activity of N-doped graphene. The highest value of $N_e$ is found for Ar−O−N (3.5), while the lowest is for N−O−Ar (2.7). Also, the low $N_e$ value for N−O−Ar is consistent with that for Ar30 ($N_e$ of 2.5). Such a contrast suggests that argon plasma treatment may create vacancy defects by removing nitrogen and oxygen dopants that are essential for 4e$^-$ ORR catalysis. In addition, the lower activity for O−Ar−N than for Ar−O−N also supports the hypothesis that vacancy introduction after oxygenation may knock out oxygen dopants, leaving fewer oxygen dopants to activate N-doped graphene for ORR. In brief, oxygenated defects predominate over other doping forms in activating N-doped graphene for ORR catalysis.

## ■ CONCLUSIONS

In summary, we used a well-defined monolayer graphene as a metal-free carbon catalyst to unveil the individual and synergy roles of nitrogen dopants, oxygen dopants, and vacancy defects for ORR. Without the presence of oxygen dopants and vacancy defects, nitrogen doping alone in graphene results in low ORR activities. The presence of trace amounts of intrinsic oxygen groups on the surface of graphene leads to an enhanced activity upon nitrogen doping. The systematic incorporation of nitrogen into graphene predoped with oxygen dopants and vacancy defects further improves the ORR activity due to synergistic effects. Especially, the presence of oxygenated defects demonstrates a significant boost in ORR activity in N-doped graphene. Further structure−activity correlations reveal that the sum atom ratios of oxygen and nitrogen dopants positively correlate to the enhanced ORR activity of doped graphene. Specifically, oxygenated vacancy defects in graphene act as an integrated center toward efficient 4e$^-$ reduction and enhanced ORR activity, which can be further boosted by nitrogen dopants by modifying the electronic nature of the doped system. We believe that our findings provide new and critical insights in the understanding of the integrated active site in complexed carbon systems and represent an important start for the rational design of highly efficient carbon catalysts.

## ■ ASSOCIATED CONTENT

**⑤ Supporting Information**

The Supporting Information is available free of charge at https://pubs.acs.org/doi/10.1021/acscatal.1c03662.

> Methods; high resolution transmission electron microscopy image and the fast Fourier transform pattern; Raman spectroscopy analysis; defect density and interdefect distance analysis; illustration schemes of graphene surface preparations; XPS C 1s core level spectra; CV analysis; ORR activities; LSV curves; Levich constant and collection efficiency; scheme of graphene lattice; XPS analysis results (PDF)

## ■ AUTHOR INFORMATION

**Corresponding Authors**

**Grégory F. Schneider** − *Leiden Institute of Chemistry, Leiden University, 2333CC Leiden, The Netherlands;* ⓞ orcid.org/0000-0001-5018-3309; Email: g.f.schneider@chem.leidenuniv.nl

**Dennis G. H. Hetterscheid** − *Leiden Institute of Chemistry, Leiden University, 2333CC Leiden, The Netherlands;* ⊙ orcid.org/0000-0001-5640-4416; Email: d.g.h.hetterscheid@chem.leidenuniv.nl

## Authors

**Lin Jiang** − *Leiden Institute of Chemistry, Leiden University, 2333CC Leiden, The Netherlands*

**Bas van Dijk** − *Leiden Institute of Chemistry, Leiden University, 2333CC Leiden, The Netherlands*

**Longfei Wu** − *Laboratory for Inorganic Materials and Catalysis, Department of Chemical Engineering and Chemistry, Eindhoven University of Technology, 5600 MB Eindhoven, The Netherlands;* ⊙ orcid.org/0000-0001-6330-3613

**Clément Maheu** − *Surface Science Laboratory, Department of Materials and Earth Sciences, Technical University of Darmstadt, 64287 Darmstadt, Germany;* ⊙ orcid.org/0000-0001-5417-5672

**Jan P. Hofmann** − *Laboratory for Inorganic Materials and Catalysis, Department of Chemical Engineering and Chemistry, Eindhoven University of Technology, 5600 MB Eindhoven, The Netherlands; Surface Science Laboratory, Department of Materials and Earth Sciences, Technical University of Darmstadt, 64287 Darmstadt, Germany;* ⊙ orcid.org/0000-0002-5765-1096

**Viorica Tudor** − *Leiden Institute of Chemistry, Leiden University, 2333CC Leiden, The Netherlands*

**Marc T. M. Koper** − *Leiden Institute of Chemistry, Leiden University, 2333CC Leiden, The Netherlands*

Complete contact information is available at:
https://pubs.acs.org/10.1021/acscatal.1c03662

## Author Contributions

L.J., G.F.S., and D.G.H.H. conceived and designed the experiments. L.J. performed all the sample preparations, characterizations, and measurements. G.F.S., D.G.H.H., and M.T.M.K. supervised and coordinated the research. L.J. analyzed the data and constructed the discussion with the support of B.v.D. B.v.D. and D.G.H.H. provided the electrochemical instrument and contributed to the electrochemical experiments and analysis. L.W., C.M., and J.P.H. did the X-ray photoelectron spectroscopy characterizations and data analysis. V.T. provided the CVD graphene samples. L.J., B.v.D., G.F.S., and D.G.H.H. wrote the manuscript. All the authors discussed the results and commented on the manuscript.

## Notes

The authors declare no competing financial interest.
The data that support the findings of this study are available from the corresponding authors on request.

## ◼ REFERENCES

(1) Gong, K.; Du, F.; Xia, Z.; Durstock, M.; Dai, L. *Science* **2009**, *323* (5915), 760−764.

(2) Shui, J.; Wang, M.; Du, F.; Dai, L. *Sci. Adv.* **2015**, *1* (1), e1400129.

(3) Ito, Y.; Qiu, H. J.; Fujita, T.; Tanabe, Y.; Tanigaki, K.; Chen, M. *Adv. Mater.* **2014**, *26* (24), 4145−4150.

(4) Qu, L.; Liu, Y.; Baek, J.-B.; Dai, L. *ACS Nano* **2010**, *4* (3), 1321−1326.

(5) Yang, H. B.; Miao, J.; Hung, S.-F.; Chen, J.; Tao, H. B.; Wang, X.; Zhang, L.; Chen, R.; Gao, J.; Chen, H. M. *Sci. Adv.* **2016**, *2* (4), e1501122.

(6) Lai, L.; Potts, J. R.; Zhan, D.; Wang, L.; Poh, C. K.; Tang, C.; Gong, H.; Shen, Z.; Lin, J.; Ruoff, R. S. *Energy Environ. Sci.* **2012**, *5* (7), 7936−7942.

(7) Wang, T.; Chen, Z.-X.; Chen, Y.-G.; Yang, L.-J.; Yang, X.-D.; Ye, J.-Y.; Xia, H.-P.; Zhou, Z.-Y.; Sun, S.-G. *ACS Energy Lett.* **2018**, *3* (4), 986−991.

(8) Guo, D.; Shibuya, R.; Akiba, C.; Saji, S.; Kondo, T.; Nakamura, J. *Science* **2016**, *351* (6271), 361−365.

(9) Wang, N.; Lu, B.; Li, L.; Niu, W.; Tang, Z.; Kang, X.; Chen, S. *ACS Catal.* **2018**, *8* (8), 6827−6836.

(10) Zheng, Y.; Jiao, Y.; Li, L. H.; Xing, T.; Chen, Y.; Jaroniec, M.; Qiao, S. Z. *ACS Nano* **2014**, *8* (5), 5290−5296.

(11) Luo, Z.; Lim, S.; Tian, Z.; Shang, J.; Lai, L.; MacDonald, B.; Fu, C.; Shen, Z.; Yu, T.; Lin, J. *J. Mater. Chem.* **2011**, *21* (22), 8038−8044.

(12) Jia, Y.; Zhang, L.; Du, A.; Gao, G.; Chen, J.; Yan, X.; Brown, C. L.; Yao, X. *Adv. Mater.* **2016**, *28* (43), 9532−9538.

(13) Lu, Z.; Chen, G.; Siahrostami, S.; Chen, Z.; Liu, K.; Xie, J.; Liao, L.; Wu, T.; Lin, D.; Liu, Y. *Nat. Catal.* **2018**, *1* (2), 156.

(14) Kim, H. W.; Ross, M. B.; Kornienko, N.; Zhang, L.; Guo, J.; Yang, P.; McCloskey, B. D. *Nat. Catal.* **2018**, *1* (4), 282.

(15) Jia, Y.; Zhang, L.; Zhuang, L.; Liu, H.; Yan, X.; Wang, X.; Liu, J.; Wang, J.; Zheng, Y.; Xiao, Z. *Nat. Catal.* **2019**, *2*, 688.

(16) Li, Q.; Zhang, S.; Dai, L.; Li, L.-s. *J. Am. Chem. Soc.* **2012**, *134* (46), 18932−18935.

(17) Cote, L. J.; Kim, F.; Huang, J. *J. Am. Chem. Soc.* **2009**, *131* (3), 1043−1049.

(18) Zhang, L.; Lin, C. Y.; Zhang, D.; Gong, L.; Zhu, Y.; Zhao, Z.; Xu, Q.; Li, H.; Xia, Z. *Adv. Mater.* **2019**, *31* (13), 1805252.

(19) Yan, X.; Liu, H.; Jia, Y.; Zhang, L.; Xu, W.; Wang, X.; Chen, J.; Yang, D.; Yao, X. *Cell Rep. Phys. Sci.* **2020**, *1* (7), 100083.

(20) Radovic, L. R.; Salgado-Casanova, A. J. *Carbon* **2018**, *126*, 443−451.

(21) Belyaeva, L. A.; Fu, W.; Arjmandi-Tash, H.; Schneider, G. g. F. *ACS Cent. Sci.* **2016**, *2* (12), 904−909.

(22) Prydatko, A. V.; Belyaeva, L. A.; Jiang, L.; Lima, L. M.; Schneider, G. F. *Nat. Commun.* **2018**, *9* (1), 4185.

(23) Zhang, L.; Yu, J.; Yang, M.; Xie, Q.; Peng, H.; Liu, Z. *Nat. Commun.* **2013**, *4*, 1443.

(24) Ferrari, A. C.; Basko, D. M. *Nat. Nanotechnol.* **2013**, *8* (4), 235−246.

(25) Ferrari, A. C.; Robertson, J. *Phys. Rev. B: Condens. Matter Mater. Phys.* **2000**, *61* (20), 14095.

(26) Eckmann, A.; Felten, A.; Verzhbitskiy, I.; Davey, R.; Casiraghi, C. *Phys. Rev. B: Condens. Matter Mater. Phys.* **2013**, *88* (3), 035426.

(27) Bruna, M.; Ott, A. K.; Ijás, M.; Yoon, D.; Sassi, U.; Ferrari, A. C. *ACS Nano* **2014**, *8* (7), 7432−7441.

(28) Das, A.; Pisana, S.; Chakraborty, B.; Piscanec, S.; Saha, S.; Waghmare, U.; Novoselov, K.; Krishnamurthy, H.; Geim, A.; Ferrari, A. *Nat. Nanotechnol.* **2008**, *3* (4), 210−215.

(29) Wang, Q. H.; Shih, C.-J.; Paulus, G. L.; Strano, M. S. *J. Am. Chem. Soc.* **2013**, *135* (50), 18866−18875.

(30) Lucchese, M. M.; Stavale, F.; Ferreira, E. M.; Vilani, C.; Moutinho, M.; Capaz, R. B.; Achete, C.; Jorio, A. *Carbon* **2010**, *48* (5), 1592−1597.

(31) Zafar, Z.; Ni, Z. H.; Wu, X.; Shi, Z. X.; Nan, H. Y.; Bai, J.; Sun, L. T. *Carbon* **2013**, *61*, 57−62.

(32) Eckmann, A.; Felten, A.; Mishchenko, A.; Britnell, L.; Krupke, R.; Novoselov, K. S.; Casiraghi, C. *Nano Lett.* **2012**, *12* (8), 3925−3930.

(33) Jiang, L.; Fu, W.; Birdja, Y. Y.; Koper, M. T.; Schneider, G. F. *Nat. Commun.* **2018**, *9* (1), 793.

(34) Suk, J. W.; Kitt, A.; Magnuson, C. W.; Hao, Y.; Ahmed, S.; An, J.; Swan, A. K.; Goldberg, B. B.; Ruoff, R. S. *ACS Nano* **2011**, *5* (9), 6916−6924.

(35) Chen, F.; Qing, Q.; Xia, J.; Tao, N. *Chem. - Asian J.* **2010**, *5* (10), 2144−2153.

(36) Zhang, C.; Fu, L.; Liu, N.; Liu, M.; Wang, Y.; Liu, Z. *Adv. Mater.* **2011**, *23* (8), 1020−1024.

(37) Schiros, T.; Nordlund, D.; Pálová, L.; Prezzi, D.; Zhao, L.; Kim, K. S.; Wurstbauer, U.; Gutiérrez, C.; Delongchamp, D.; Jaye, C. *Nano Lett.* **2012**, *12* (8), 4025−4031.

(38) Li, J.; Lin, L.; Rui, D.; Li, Q.; Zhang, J.; Kang, N.; Zhang, Y.; Peng, H.; Liu, Z.; Xu, H. *ACS Nano* **2017**, *11* (5), 4641−4650.

(39) Blizanac, B.; Ross, P.; Markovic, N. *Electrochim. Acta* **2007**, *52* (6), 2264−2271.

(40) Sarapuu, A.; Helstein, K.; Vaik, K.; Schiffrin, D. J.; Tammeveski, K. *Electrochim. Acta* **2010**, *55* (22), 6376−6382.

(41) Daems, N.; Sheng, X.; Vankelecom, I. F.; Pescarmona, P. P. *J. Mater. Chem. A* **2014**, *2* (12), 4085−4110.

(42) Wang, X.; Jia, Y.; Mao, X.; Zhang, L.; Liu, D.; Song, L.; Yan, X.; Chen, J.; Yang, D.; Zhou, J. *Chem.* **2020**, *6* (8), 2009−2023.

(43) Liu, X.; Dai, L. *Nat. Rev. Mater.* **2016**, *1* (11), 16064.

(44) Tang, L.; Ji, R.; Li, X.; Teng, K. S.; Lau, S. P. *J. Mater. Chem. C* **2013**, *1* (32), 4908−4915.

(45) Kim, H. W.; Bukas, V. J.; Park, H.; Park, S.; Diederichsen, K. M.; Lim, J.; Cho, Y. H.; Kim, J.; Kim, W.; Han, T. H. *ACS Catal.* **2020**, *10* (1), 852−863.